CHALMERS
UNIVERSITY OF TECHNOLOGY

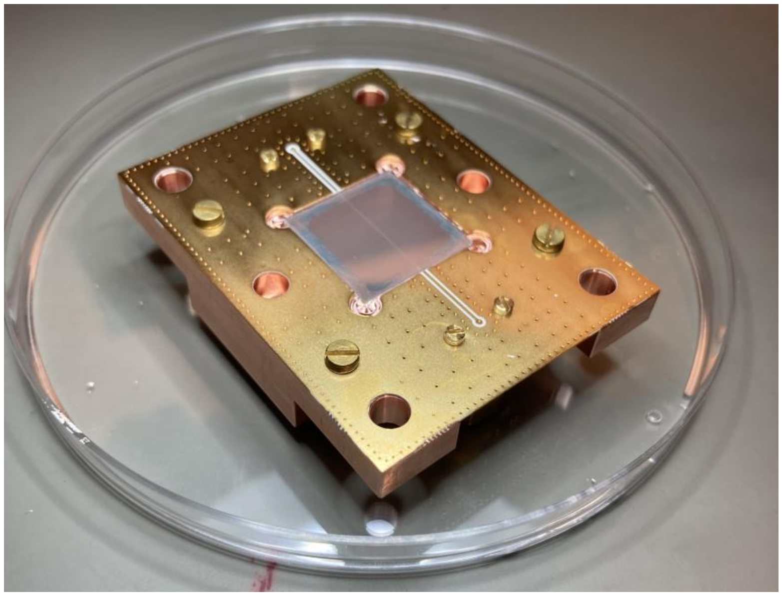

Quantum Limited Amplifier

Design, Fabrication and Characterization of a Superconducting NbTiN Kinetic Inductance Travelling Wave Parametric Amplifier

TRA105: Building and Programming a Quantum Computer

December 2021

Núria Alcalde-Herraiz herraiz@student.chalmers.se
Linus Andersson anlinus@student.chalmers.se
Ivan Hagström hivan@student.chalmers.se
Paul Jamet Suria jamet@student.chalmers.se

Project Supervised by: Attila Geresdi and Simone Gasparinetti

With the Assistance of: Robert Rehammar, Mikael Kervinen, François Joint, Ivo Cools, Vittorio Buccheri, Lars Jönsson

CHALMERS UNIVERSITY OF TECHNOLOGY
Gothenburg, Sweden 2021
www.chalmers.se

Abstract

The aim of this project was to design, fabricate and characterize a kinetic inductance travelling wave parametric amplifier (KI-TWPA) for cryogenic temperatures (10 mk) by adapting the design of Malnou et.al PRX Quantum (2020) [1] for a sapphire substrate of 430 µm. By utilizing the properties of periodic structures in a transmission line, the dispersive properties of the device could be modified, enabling phase matching of the signal and pump frequencies. The pattern was designed on Klayout, simulated in Sonnet[2] and fabricated in Chalmers MC2 cleanroom by sputtering of NbTiN, Electron beam lithography and Reactive ion etching.

Additionally, a cryogenic microwave packaging was designed and fabricated. The packaging consists of a PCB designed in KiCad and a copper box designed in Autodesk Inventor. The PCB consists of two copper layers with Rogers RO4350B dielectric material in between the layers. The transmission line showed good matching in the frequency region of importance. When designing the copper box, the dominant cavity and chip resonant frequencies were engineered to exist outside the band of operation. The microwave properties of the PCB and copper box were simulated using COMSOL[3].

The superconductive device was measured at cryogenic temperatures and important device parameters were characterised. In particular, the kinetic inductance of the sample was characterised as well as the critical current of the device. The order of non-linearity was found to be $I_* =$ 7.33 - 8.26 mA and the critical current $I_c = 2.2$ mA. Through measurements of the transmission, the passband and stopband characteristics of the periodic structure were obtained. Thus, acquiring key parameters for the device. Due to fabrication issues, only one of the samples with a shorter amplification path could be measured. Therefore, signal gain could not be observed on the measured device since the gain is heavily dependant on the length of the transmission line.

Contents

1 Introduction

As the field of quantum computing evolves the need for high gain, low noise microwave amplifiers grows. Qubit state readout requires microwave probing of coupled superconducting resonators at very low power levels (a few photons) in order to maintain the coherence of the quantum state. The generated microwave signals require low noise pre-amplification at the lowest stage of a dilution refrigerator cryostat, around 10 mK, before thermal noise increases further up the column [4]. A common approach for this application is the use of traveling wave parametric amplifiers. Their noise performance approaches the quantum limit while maintaining low power dissipation (<10 µW), below the cooling power of the cryostat. In traveling wave parametric amplifiers the input signal propagates trough a transmission line while periodically interacting and drawing energy from a pump signal inside a non-linear medium [5]. For microwave parametric amplification, the role of the non-linear medium can be played by the non-linear inductance of a superconducting circuit. The two main candidates of non-linear mediums are high kinetic inductance disordered superconducting thin films such as NbTiN [1], [6], [7]and Josephson junctions [4]. This project focuses on the former as we benefit from the developments in deposition and patterning of NbTiN thin films made by the supervisor Attila Geresdi.

The aim of this project is to study a kinetic inductance traveling wave parametric amplifier through the reproduction of a device created by Malnou et.al in [1]. Therefore, the scope contemplates the design, fabrication and characterization of the device as well as the design and fabrication of suitable packaging for microwave amplification inside a dilution refrigeration cryostat.

2 Theoretical Background

This section aims to provide the principles of a kinetic inductance traveling wave amplifier and the necessary microwave theory. A brief theoretical background on superconductivity will be given to establish a solid basis on the kinetic inductance concept. Afterwards, the basics of transmission lines theory are covered, describing typical parameters to characterize them. Next, the properties of periodic structures in transmission lines are explained to conclude on parametric amplification. Finally, a brief overview of resonant cavities is given.

2.1 From Superconductivity to Kinetic Inductance

A metal in the normal state is formed by a gas of repulsive electrons as described in Drude model [8]. This model allows to define the metal conductance under a DC field as:

$$\sigma_n = \frac{n_n \tau e^2}{m_e} \tag{1}$$

where τ is the time elapsed between scattering events in the electron gas. Although when the material is cooled below a critical temperature, T_c, the Coulomb forces that repel the electrons are counteracted by additional attractive forces. The pair formation between electrons becomes energetically advantageous, consequently, possible [9]. The union between the two electrons is called a Cooper pair, however, due to the scope of this work we are going to refer to them as superconducting electrons. Therefore, a superconductor can be described as material that below T_c presents both normal and superconducting electrons. This superconductivity picture is formally called the two-fluid model and was formulated by Gorter and Casimir [10]. It proposes that each type of electrons constitute a fluid that flows inside the material and has certain characteristics. The normal electrons carry entropy, present scattering and have normal conductance, whereas the superconducting electrons have no scattering, no entropy, and infinite conductance. As each kind of electron constitutes a fluid, they are treated as densities of electrons, with n_n being the normal one and n_s the superconducting one. The presence of each fluid inside the material is not binary when reaching T_c. Instead, it follows the ratio:

$$\frac{n_s}{n} = 1 - \left(\frac{T}{T_c}\right)^4 \tag{2}$$

where n is the total electron density.

Intuitively, when a DC current is applied below T_c it will be carried by the superconducting electron fluid, as it is non-dissipative. However, a further mathematical analysis of the conduction involves the normal electron fluid for low-frequencies [11], [12] as observed in:

$$\sigma = \frac{n_n \tau e^2}{m_e(1+w^2\tau^2)} - i\left(\frac{n_n \tau w e^2}{m_e(1+w^2\tau^2)} + \frac{n_s e^2}{m_e w}\right), \tag{3}$$

where w is the frequency of the applied signal. For frequencies in the microwave regime ($w\tau \ll 1$) and a temperature far from T_c ($n_n \ll n_s$),(3) turns into:

$$\sigma = \frac{n_n e^2}{m_e} w\tau^2 - i\left(\frac{n_s e^2}{m_e w}\right)$$

Note that the real term of the equation can be substitute by Drude DC conductivity (1):

$$\sigma = \sigma_n \frac{n_n}{n} - i\left(\frac{n_s e^2}{m_e w}\right) \tag{4}$$

To further understand the implications of the equation above, we have to extend the description of superconductivity, as so far, a superconductor can be mistaken by a perfect metal. However, these materials are also perfect diamagnets. Below T_c, when an external magnetic field is applied to the material, it does not penetrate it, as screening currents flowing on the metal surface counteract it [11], [12]. This is known as the Meissner Effect [13]. It is this extension that shows that the superconducting state is a true thermodynamic equilibrium state. The same way it was energetically convenient for the material to form the superconducting electrons under T_c, it is also energetically convenient for the superconductor to repel the applied field creating the screening current. However, there is a limit to how much you can increase the applied magnetic field, in other words, how much one can increase the screening current. Until this point, we have a full image of superconductivity, a thermodynamic state limited by a critical temperature, T_c, and a critical field, B_c, a critical current, I_c.

The first superconductivity theory that contemplated magnetic fields was developed by Fritz and Heinz London [11], [12]. Their description relates the microscopic electric and magnetic fields inside superconductors which allowed to quantify the screening current and the region where it flows. Furthermore, it leads to the definition of the London penetration depth, λ_L. Which is the region where the screening current flows canceling the magnetic field that decays exponentially. The London penetration depth is defined as:

$$\lambda_L = \sqrt{\frac{m_e}{\mu_0 n_s e^2}} \tag{5}$$

which is also a temperature dependent parameter due to n_s. It is possible to relate (4) and (5):

$$\sigma = \sigma_n \frac{n_n}{n} - i\left(\frac{1}{\mu_0 w \lambda_L}\right) \tag{6}$$

(6) presents a similar structure as an impedance with a resistive and inductive term: $Z^{-1} = R^{-1} + (iwL)^{-1}$. Thus, we can extend the description of a superconducting material as a parallel RL circuit.

As a recap, the description of a superconductor material has been provided and its conductivity in the microwave regime and a temperature far from T_c enabled to model the material as a RL circuit. Thus, our current scenario takes into account a microwave signal and an inductive circuit. Physically, this model can be understood by analyzing the interaction between the microwave signal and the normal and superconducting electrons. When such signal interacts with the superconductor, the time-varying electric field accelerates the charge carrying normal electrons and a dissipation event takes place, resulting in the resisting term of (6). But the non-dissipating superconducting electrons will also be accelerated. However, the superconducting electrons need time to be accelerated to their final velocity, thus, a delay of the current with respect to the voltage occurs. This delay is the one that reflects the inductive behavior of the electrons, imaginary term of (6). As its cause is the inertial mass of the superconducting electrons under an alternating field, the inductance is named kinetic inductance L_k. The total inductance of a superconductor L is the sum of its geometric inductance L_G and kinetic inductance L_k. However, for highly resisting superconductors made into high critical current density structures, as NbTiN, L_k can exceed 90% of the total inductance [1], [7], which allows to describe the L as:

$$L(I) = L_0\left[1 + \frac{I^2}{I_*^2}\right] \tag{7}$$

where the I_* is the scaling parameter of the order of the critical current and L_0 is the total inductance (kinetic and geometric) of a thin film with thickness t smaller than the London penetration depth ($t \ll \lambda_L$) under no current bias.

In the following sections it will be described how a kinetic inductance traveling wave parametric amplifier makes use of the non-linearity showed in (7) to obtain gain.

2.2 Transmission Lines

When analyzing high frequency circuits, it is not sufficient to use the lumped element model when describing the voltages and currents in a circuit. If the wavelength of the signals is approaching the dimensions of the circuit, the magnitude and phase difference along the circuit elements must be considered [14, pp.48].

Consider a lossless transmission line, described by a series inductance per unit length L (H/m) and a shunt capacitance per unit length C (F/m). Kirchhoff's voltage and current laws does not immediately apply to the description of a transmission line, since they assume constant magnitude and phase along each element. However, by considering an infinitesimal section of the transmission line, Kirchhoff's laws can still be used to derive the high frequency characteristics of a transmission line. Assuming harmonics signals, this way of reasoning results in the voltage and current wave equations

$$\frac{\partial^2 V(z)}{\partial z^2} - \gamma^2 V(z) = 0 \tag{8}$$

$$\frac{\partial^2 I(z)}{\partial z^2} - \gamma^2 I(z) = 0 \tag{9}$$

derived from the *telegrapher equations*, where $\gamma = j\omega\sqrt{LC}$ is the propagation constant for a lossless transmission line [14, pp.50]. These equations have the solutions

$$V(z) = V_0^+ e^{-\gamma z} + V_0^- e^{\gamma z}$$

$$I(z) = I_0^+ e^{-\gamma z} + I_0^- e^{\gamma z}$$

describing forward and backwards traveling voltage and current waves.

An important parameter of the transmission line is the characteristic impedance

$$Z_0 = \frac{V_0^+}{I_0^+} = \frac{V_0^-}{I_0^-} = \sqrt{\frac{L}{C}} \tag{10}$$

relating the voltage and current in the transmission line. As a consequence of the electromagnetic boundary conditions, the voltage and currents will be partially reflected if the transmission line is terminated with a load $Z_L \neq Z_0$ [15, pp.397-400]. The amount of the incoming wave that is reflected is described by the reflection coefficient

$$\Gamma = \frac{V_0^-}{V_0^+} = \frac{Z_L - Z_0}{Z_L + Z_0} \tag{11}$$

at the termination interface.

2.3 Scattering Parameters and ABCD Matrices

Scattering parameters (S-parameters) can be used to characterize any N-port microwave network [14, pp.178]. For a 2-port network, the S-matrix is defined as

$$\begin{bmatrix} V_1^- \\ V_2^- \end{bmatrix} = \begin{bmatrix} S_{11} & S_{12} \\ S_{21} & S_{22} \end{bmatrix} \begin{bmatrix} V_1^+ \\ V_2^+ \end{bmatrix}$$

where the stimulus is the incoming voltage waves $[V_1^+, V_2^+]$ with the response $[V_1^+, V_2^+]$. S_{11} and S_{22} is the input and output reflection coefficients, while S_{12} and S_{21} is the transmission of the 2-port network.

When cascading 2-port networks, it can sometimes be easier to work with ABCD-parameters (also known as voltage-current parameters) instead of S-parameters. The ABCD-parameters is defined as

$$\begin{bmatrix} V_1 \\ I_1 \end{bmatrix} = \begin{bmatrix} A & B \\ C & D \end{bmatrix} \begin{bmatrix} V_2 \\ I_2 \end{bmatrix}$$

where $[V_1, I_1]$ and $[V_2, I_2]$ is the voltage and current on the input and output of the 2-port respectively [16, pp.257-259].The equivalent ABCD-matrix of several cascaded 2-port networks is the matrix multiplication of the ABCD-matrix for each 2-port. Once the ABCD-matrix of the 2-port is known, it is possible to transform ABCD-parameters to S-parameter representation. The transmission S_{21} and reflection S_{11} are then found by the following transformations.

$$S_{21} = \frac{2}{A + B/Z_0 + CZ_0 + D}, \tag{12}$$

$$S_{11} = \frac{A + B/Z_0 - CZ_0 - D}{A + B/Z_0 + CZ_0 + D}. \tag{13}$$

2.4 Periodic Structures and Artificial Transmission Lines

Periodic structures in transmission lines or waveguides consisting of reactive elements have the property of showing passband-stopband characteristics [16, pp.550]. To analyze these types of structures they are divided into sub-circuits, called unit cells, each described by an ABCD-matrix. Using the cascading properties of ABCD-matrices described in 2.3, the overall ABCD-matrix of the structure can be found.

Consider a transmission line such as a coplanar waveguide (CPW). The transmission line has a characteristic impedance Z_0 given by its inductance and capacitance per unit length shown in (10). The equivalent circuit of CPW can be thought of as a series inductance and a shunt capacitance to ground. By modifying the CPW, it is possible to create a periodic structure that is referred to as an artificial transmission line, described by equivalent lumped components. Hence, an ABCD-matrix can be constructed from the lumped element circuit.

By describing a periodic pattern of a CPW in terms of unit cells, it can be modified to achieve the desired passband and stopband characteristics. This is called impedance loading and it can be used to affect the transmission properties of the waveguide. Finally, when the overall ABCD-matrix of the structure is known, the S-parameters can be found according to (12),(13).

The kinetic inductance traveling wave parametric amplifier (KI-TWPA) developed in this project uses periodic impedance loading of an artificial waveguide to create a periodic structure, similar to a photonic crystal, with a bandgap or stopband in the desired frequency range.

2.5 Parametric Amplification

In a traveling wave parametric amplifier (TWPA), a signal with frequency f_s travels through a transmission line where it can interact with a pump frequency f_p. Through mixing, some of the pump's energy can be transferred to the signal frequency through an idler frequency f_i, thus amplifying it. A TWPA needs two conditions fulfilled to work: energy conservation and momentum conservation[7].

Energy conservation can be established either through four-wave mixing (4WM) or three-wave mixing (3WM). In 4WM we have $2f_p = f_s + f_i$ where two pump photons are transformed into one signal photon and one idler photon, while in 3WM $f_p = f_s + f_i$ where a single pump photon are transformed into both signal and idler photons. However, for 3WM a DC bias is needed[7].

If we take (7), the inductive energy of the TWPA can be calculated with the kinetic inductance as follows[7].

$$I = I_{DC} + I_{RF}, \tag{14}$$

$$\begin{aligned} L(I) &= L_0 \left[1 + \frac{I^2}{I_*^2}\right] \\ &= L_0 \left[1 + \frac{I_{DC}^2 + 2I_{DC}I_{RF} + I_{RF}^2}{I_*^2}\right], \end{aligned} \tag{15}$$

$$\begin{aligned} E(I) &= \frac{1}{2} L I_{RF}^2 \\ &= \frac{1}{2} L_0 \left[\left(1 + \frac{I_{DC}}{I_*^2}\right) I_{RF}^2 + 2\frac{I_{DC}^2}{I_*^2} I_{RF}^3 + \frac{1}{I_*^2} I_{RF}^4\right], \end{aligned} \tag{16}$$

where I_{DC} and I_{RF} are the DC and the RF currents and I_* now represents a characteristic constant of the TWPA that determines the scale of non-linearity. In equation (16) the second term enables 3WM and the third term enables 4WM. Notably, the third term is zero when no dc-current is applied. Hence the need for a DC bias in 3WM.

There are two main advantages of using 3WM over 4WM. Firstly, because the pump frequency is approximately twice the signal frequency (when the signal and idler frequencies are of the same order of magnitude) it can easily be filtered out with a low-pass filter. Secondly, with the additional cubic term in I_{RF} a smaller RF current is necessary to achieve the same gain than in the 4WM case. This reduces the additional noise from heat dissipation caused by large RF power[1][7].

To establish momentum conservation we need phase-matching. The phase-matching condition can be derived by inserting the kinetic inductance in equation (15) into the telegrapher equations, under the condition that $f_p = f_s + f_i$[1]. The differential equations can then be solved if

$$\Delta\kappa = -\frac{|I_p|^2}{8} \frac{1}{I_*^2 + I_{DC}^2} (k_p - 2k_s - 2k_i), \tag{17}$$

$$\Delta\kappa = k_p - k_s - k_i, \tag{18}$$

where k_j, j $\in \{p, s, i\}$ are the pump, signal and idler wavenumbers and I_p is the pump current. If the phase matching condition is fulfilled we get a signal current of the form

$$I_s = \cosh(g_3 x) I_0, \tag{19}$$

$$g_3 = \frac{1}{8}\delta_L k_p \tag{20}$$

where δ_L is the relative inductance variation due to the pump signal and phase factors have been omitted. The gain can then be calculated as

$$G_s(x) = \left|\frac{I_s(x)}{I_0}\right|^2 = \cosh^2(g_3 x) \tag{21}$$

The gain is then exponential in the length of the transmission line, x.

2.6 Cavity Resonances

Stepping aside from transmission lines, this section provides a brief reminder about cavity resonances due to its interest in the cryogenic microwave packaging design. In particular, it is important to remember the frequency resonant modes of a rectangular cavity.

In a rectangular cavity of dimensions $b < a < d$, there are resonant modes of frequencies

$$f_{mnl} = \frac{c_0}{2\pi\sqrt{\epsilon_r \mu_r}} \sqrt{\left(\frac{\pi m}{a}\right)^2 + \left(\frac{\pi n}{b}\right)^2 + \left(\frac{\pi l}{d}\right)^2}, \tag{22}$$

where m, n, l are integers, c_0 is the speed of light in vacuum and ϵ_r and μ_r are the relative permittivity and permeability of the medium in the cavity, respectively. The lowest frequency mode is for a TE_{101} wave [14].

3 Design and Fabrication

The following section focuses on the design of both the KI-TWPA and the cryogenic microwave packaging composed of a printed circuit board (PCB) and a copper box. The first subsection centers on the description of the reference design from Malnou et.al [1] and the adaptations to our final design, as well as the fabrication process. The second subsection will discuss the key parameters of the design of both the PCB and copper box.

3.1 KI-TWPA

3.1.1 KI TWPA Design in Malnou et al.

As previously mentioned, the amplifier is an artificial transmission line made of a nonlinear medium (high KI) along which two tones (signal and pump) propagate and exchange energy. For efficient 3WM amplification, pump depletion, a phenomena due to the presence of other parametric conversion processes other than 3WM with the pump [7], needs to be avoided. In order to avoid these processes the transmission line is engineered to be slightly dispersive so that the phase matching condition described in section 2.5 necessary for these parametric processes is lost as the signals travel along the line.

The strategy to introduce slight dispersion at low frequency is to design an interdigitated CPW (iCPW) (see Figure 1a), this is an artificial transmission line of impedance $Z = \sqrt{L_d/C}$ where the perpendicular fingers act as low-Q $\lambda/4$ resonators at high frequency ($1/\sqrt{L_f C/2} = 2\pi \times 36$ GHz). The low-Q resonance will create a phase shift at 36 GHz that will leak into the lower frequencies thus introducing a slight dispersion. This dispersion corresponds to the dashed line in Figure 1b where k^* is the phase change introduced by each unit cell (one finger).

Notice that the dispersive line does not allow 3WM as the phase pickup along the path is different for the pump and signal. In order to retrieve the phase matching conditions for 3WM only, Malnou et al. make use of periodic loading in the line by periodically reducing the capacitance by shortening the fingers. As seen before, periodic loading in a transmission line creates a stopband at a certain loading frequency with a corresponding phase shift. By tuning the loading periodicity the location of the phase shift (and stopband) can be placed between the signal and pump frequencies thus compensating for the dispersion and retrieving the phase matching conditions for 3WM only. This particular dispersion relation suppresses through mismatching all other conversion processes other than 3WM. Figure 1b shows the new dispersion relation (black line). Note that there is only a single set of $\{k_s, k_i, k_p\}$ for which the exponential gain condition for 3WM in equation (17) is fulfilled.

Malnou et al. designed a TWPA with a periodic unit cell - called supercell - of sixty long 102 µm fingers followed by a loading sequence of six 33.5 µm fingers. Both the center line and the fingers of the iCPW are 1 µm wide and the gap to the ground plane is 1 µm as well. For this design patterned on NbTiN thin film on silicon substrate the obtained inductances and capacitances from the circuit model are: $L_d = 45.2$ pH, $L_u = 1.02$ nH, $L_l = 335$ nH, $C_u = 18.8$ fF and $C_l = 7.1$ fF. The indices u and l refer to the unloaded (102 µm) and loaded (33.5 µm) fingers. The impedances of the unloaded and loaded fingers are: $Z_u = 50\ \Omega$ and $Z_l = 80\ \Omega$.

Having understood the original design from [1] we attempt to replicate a modified design adapted to a sapphire substrate.

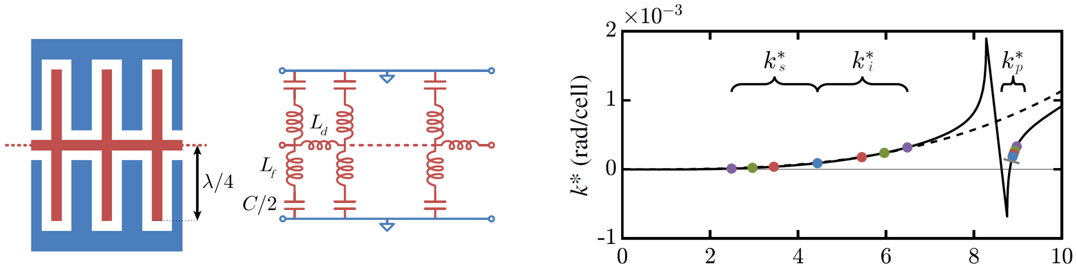

(a) (b)

Figure 1: (a) Scheme of the iCPW design along with the equivalent circuit diagram. (b) Phase shift per unit cell in a slightly dispersive interdigitated CPW with (solid line) and without (dashed line) periodic loading. Adapted from [1]

3.1.2 KI-TWPA Design Adaptation

Translating the theoretical iCPW into a pattern presented various challenges. Modifying the substrate would change the dielectric constant thus the capacitance, wheater tuning thickness of the thin film would modify the kinetic inductance of the film. In our device, the two previous situations were faced, thus the impedance of the line 10 was tuned. There were two major variations that affect directly the impendance of the line: the change of substrate, from silicon 380 µm thickness to sapphire 430 µm thickness; and the change of the NbTiN thin film fabrication, deposition of 6-7 nm insted of 20nm. However, the important parameter for NbTiN was not the thickness of the thin film per se, but the kinetic inductance per square which was the same for both the paper reference and ours: 10 pH/square. The new substrate though affect the capacitance of the unit cells enough to investigate quantitatively the impedance variation.

The periodicity of the pattern was used for this purpose as it allowed to analyze the impedance mismatch of the sections of the supercell, in particular, the sixty unloaded (102 µm long) fingers was used. The analysis was carried through using KLayout, to design the pattern, and Sonnet [2], to run the simulations. The results were evaluated using as a criteria the S11 parameter, considering a good signal transfer if it was under −20 dB, and the impedance matching, evaluated through the Smith Charts of the signals as they provided an insight of reactance of the line [16].

The first step into the impedance mismatch analysis was to characterize the affect caused by the sapphire substrate. We simulated the sixty unit cell pattern of NbTiN thin film with 10 pH/square kinetic inductance per square and the same geometrical parameters described on [1] on a silicon 380 µm and a sapphire 430 µm substrate. The result of the simulations is observed in Figure 2 where there is a right shift on the impedance matching frequency peak from 5.73 GHz to 6.50 GHz. Furthermore, the reflection of the line increased around 10 dB. It can also be observed in the inset that the impedance matching is worsened by the new sapphire substrate.

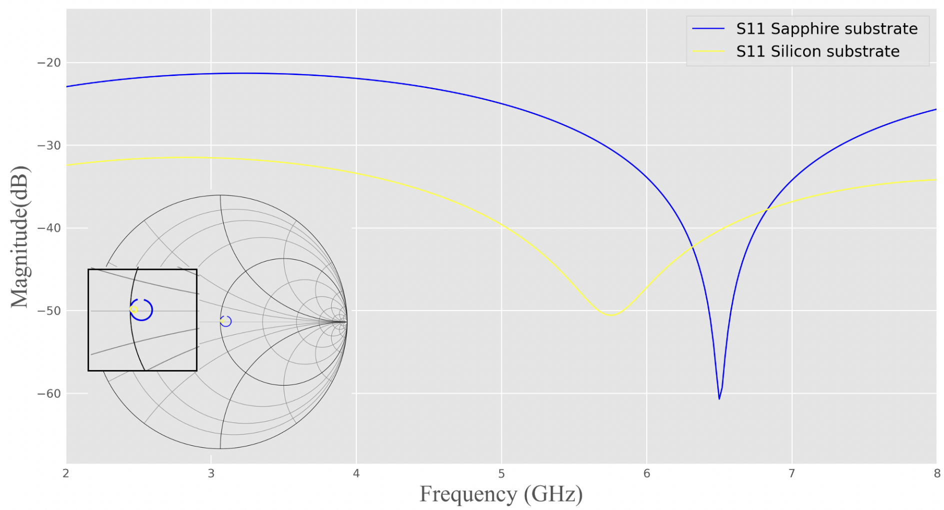

Figure 2: Comparison between the S11 response of sixty unit cells cascaded on silica 380 µm (yellow) and sapphire 430 µm (blue) substrate. Inset: Smith chart of the impedance matching to 50 Ω.

Figure 2 represents the start point of our adaptation as a better signal response was sought for a finest amplifier performance. Once the NbTiN kinetic inductance per square is settled to 10 pH/square and the substrate to sapphire 430 µm, the parameters left to be tuned are the geometric ones. Figure 3 displays a unit cell with the parameters kept from the Malnou article and the ones adjusted to find the best impedance matching for the new substrate. The parameters were: the distance between planes, d; the length of the fingers, l; and the width of the central line, w. The following section covers the result of the parameters modifications and the final pattern proposed.

The distance between planes, d, was the first parameter to be tuned. The result can be observed in Figure 4 S11. Compared to d= 1 µm from the original article, the pattern with d= 0.5 µm offered a similar matching frequency, 6.48 GHz close to 6.50 GHz, and a decrease on S11 of around 5 dB. The Smith chart inset proves that this pattern increases the capacitance of the line. However, when increasing the d to 1.5 µm the matching impedance frequency peak shifts to the right, until 7.26 GHz and the performance of the unit cells worsens S11 surpassing the −20 dB for frequencies inferiors to 5.59 GHz. Furthermore, the Smith Chart shows that the behaviour of the line tends to be more capacitive than inductive.

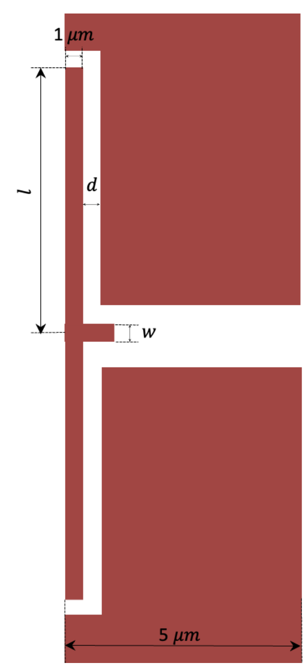

Figure 3: Unit cell of the designed TWPA with key parameters l,w,d indicated.

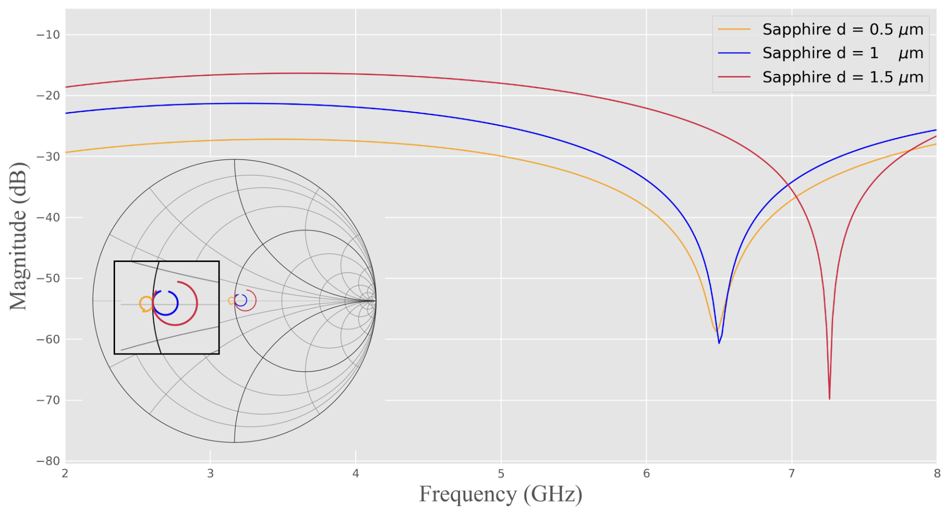

Figure 4: Comparison between the S11 response of sixty unit cells cascaded on sapphire 430 µm substrate for different d=0.5 µm (orange), 1 µm (blue), 1.5 µm (crimson). Inset: Smith chart of the impedance matching to 50 Ω.

In order to improve our matching impedance, the following parameters to be changed were w and l. Figure 5 illustrates some of these variations against the initial parameters (blue curve). The yellow S11 curve shows that while increasing l to 152 µm shifts the matching impedance frequency peak to 4.98 GHz, the S11 performance worsens. In order to correct it, l was kept at 152 µm and d was once again reduced to 0.5 µm, pink curve. However, the results were non-satisfactory as once again while shifting to the left the matching impedance frequency peak, 4.98 GHz, the S11 reflection increased. Finally, the crimson curves shows the result of increasing w from 1 µm to 2 µm which did not offered any advantage respect the aforementioned modifications as it shifted the matching peak to 7.30 GHz.

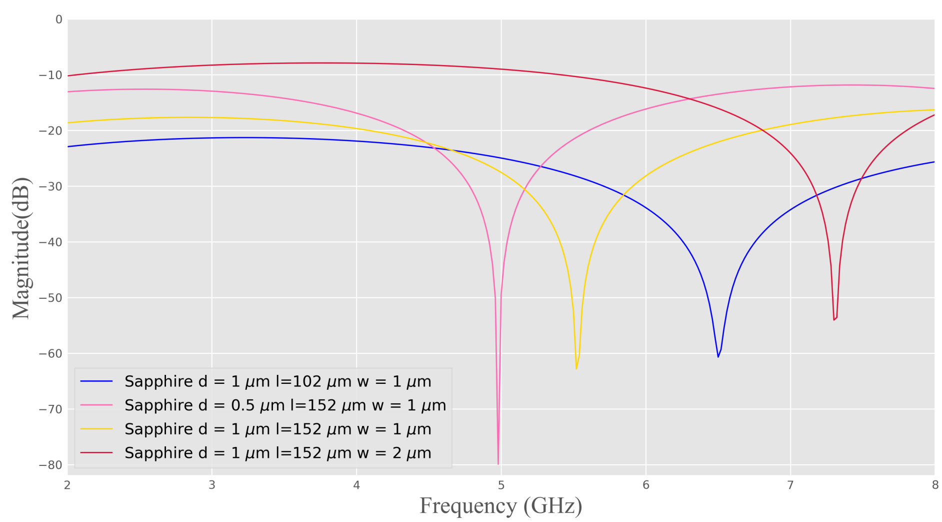

Figure 5: Comparison between the S11 response of sixty unit cells cascaded on sapphire 430 µm substrate for different geometric parameters.

All proven parameters and discussed results are shown in Table 1. In conclusion, neither varying the length of the fingers, l, or the width of the central line, w, did not outperformed the result on just reducing the distance between planes, d, to 0.5 µm.

Substrate	d **(µm)**	l **(µm)**	w **(µm)**	**Matching Peak frequency** (GHz)	<dB
Silicon	1	102	1	5.73	-20
Sapphire	1	102	1	6.50	-30
Sapphire	0.5	102	1	6.48	-25
Sapphire	1.5	102	1	7.26	-15
Sapphire	0.5	152	1	4.98	-10
Sapphire	1	152	1	5.51	-15
Sapphire	1	152	2	7.30	-5

Table 1: Collection of all the relevant data of the Sonnet simulations for sixty cascaded unit cells with expected matching impedance 50 Ω. The first column indicates the substrate used, it is implied the thicknesses of each substrate 380 µm for silicon and 430 µm for sapphire. The second to third tuned parameters indicated in Figure 3; the forth column provides information about the impedance matching peak and the later under how many decibels S11 was founded.

3.1.3 Proposed Patterns

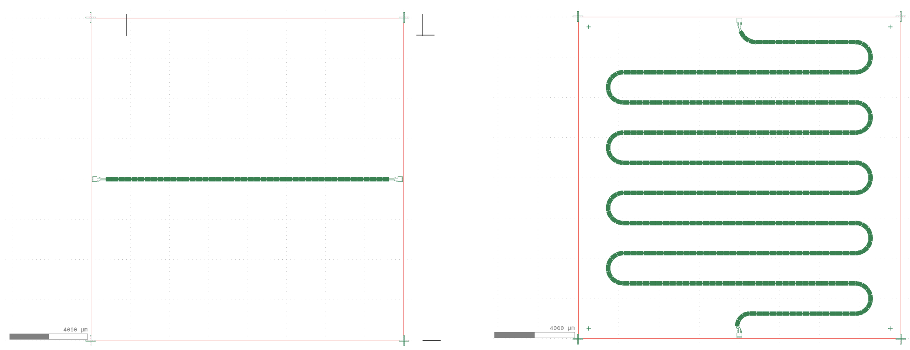

(a) (b)

Figure 6: KLayout patterns proposed for nanofabrication. (a) Test straight line pattern composed by 43 supercells and one sixty large unitcells to enable impedance matching. (b) Zig-zag pattern composed by 379 supercells.

The adapted supercell had same geometrical the parameters of Malnou et.al.[1] with an adapted distance between planes l of 0.5 µm. Hence, it was build cascading sixty unloaded (102 µm long) unit cells and six loaded (33 µm long) unit cells to create the desired stop-band response observed in section 3.1.1.

There was another modification concerning the chip size between Malnou et.al.[1] and ours. On the paper a 2 cm by 2 cm chip is used, whereas our chip was cut down to 1.6 cm by 1.6 cm. Therefore, the 33 cm length of the transmission line could not be maintained. This new amplifier feature potentially reduces the gain as observed in (21). After consideration, the two patterns observed in Figure 6 were the ones proposed to nanofabricate.

Figure 6a displays a basic straight line pattern composed by forty three supercells and sixty unloaded unit cells to enable impedance matching. Through the supercell Sonnet result and the rf-scikit python library, the S21 response of this first pattern was obtained with the stopband peak at 6.3 GHz (see Figure 3) .

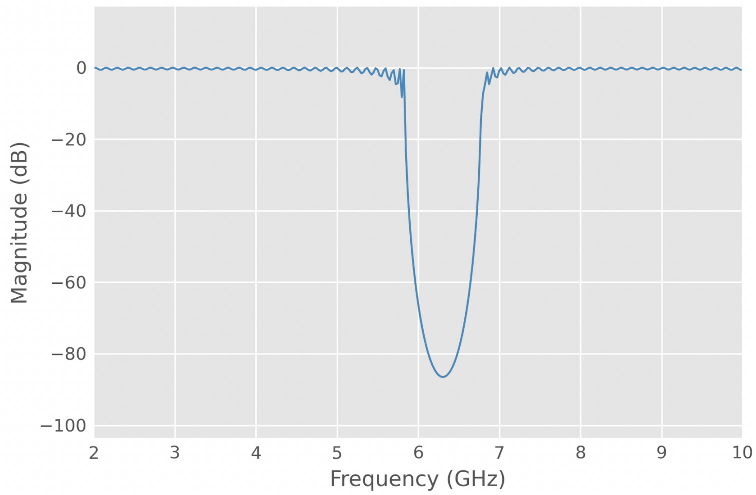

Figure 7: S21 SONNET simulation and rf-scikit result for 44 cascaded supercells.

However, this pattern was supposed to act as a test structure for the second one. Presented on Figure 6b the second pattern is 12.5 cm long, 379 supercells cascaded. Due to limitations on the computing RAM, the affect of the line bend could not be qualitatively analyzed, thus, no S21 performed could be computed. However, it is expected an increase of the reflection as is showed in Figure 8 where a six cascaded unloaded (l=33 cm) unit cells without bending (orange curve) is plotted against the same bent pattern (green curve). The inset motivates to argue that the reason is due to an increase in the inductance of the pattern.

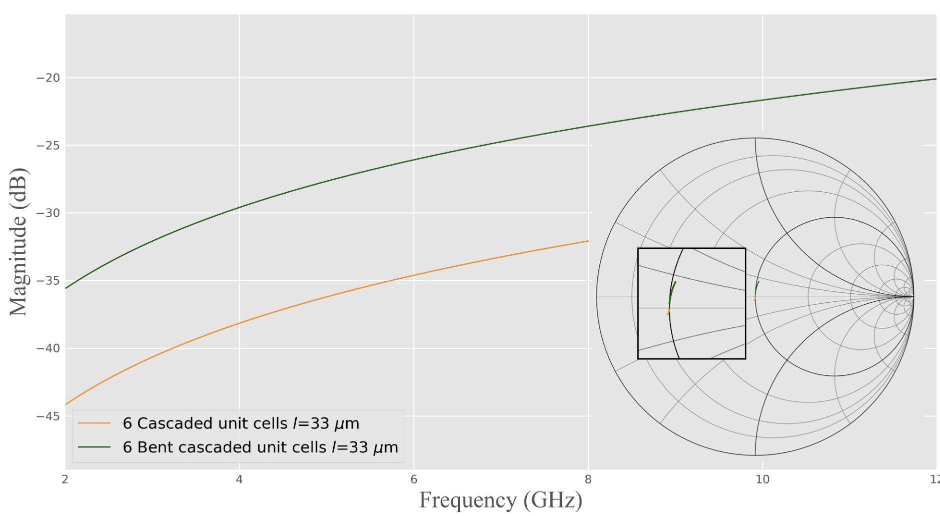

Figure 8: Comparison between the S11 response of six short unit cells non-bent (orange) and bent pattern (green). Inset: Smith chart of the impedance matching to 80 Ω.

3.1.4 Matching coplanar wave guide 50 Ω

There is one last attribute of our pattern to discuss. Once the amplifier design was decided and the model build through KLayout, a way to connect our amplifier and the measuring pads was required. In order to do so a coplanar waveguide was designed to match the PCB 50 Ω impedance as observed in Figure 6. Following a similar approach that in the previous sections for the supercell KI-TWPA, the dimensional parameters of the CPW were tuned to match the impedance.

Figure 9a helps to illustrate the established approach to design CPW, which is to fix one of a or b parameters and turn the remaining one. In Figure 9b it can be observed that this approach was not applicable to our device, when fixing the a parameter and modifying b the impedance matching was tuned until b reach a certain thickness: the same impedance was obtained for $b = 2\,\mu\text{m}$ and $b = 3\,\mu\text{m}$. However, a certain recurrence was observed as the values were incremented by a multiple of four the impedance of the CPW seemed to approach the 50 Ω. Different values of the a, b parameters using this recurrence can be observed on Figure 9c as well as the final CPW parameters chosen: a= 16 µm and b=32 µm.

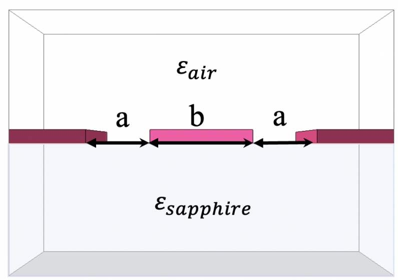

(a)

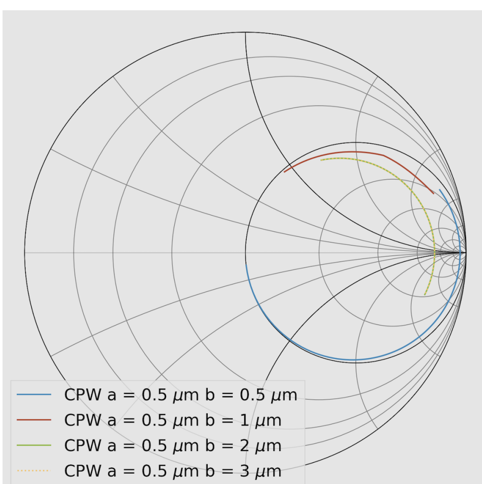

(b)

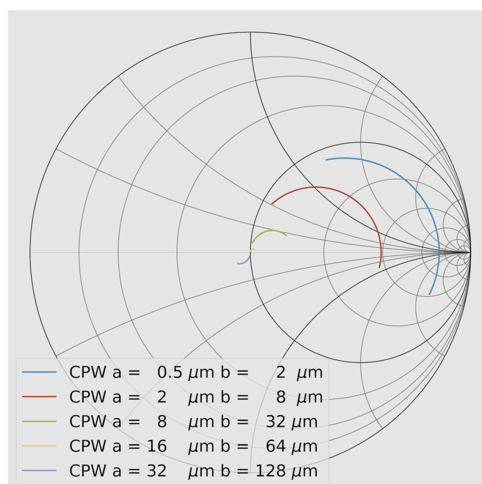

(c)

Figure 9: (a) Front view of a general CPW with the a and b parameters to be tuned indicated. (b) Smith chart of the impedance matching for the S11 signal of CPW in (a) with same a parameter and b=0.5,1,2,3 µm . (c) Smith chart of the impedance matching for the S11 signal of CPW in (a) with a quadruple ratio.

3.1.5 KI-TWPA Fabrication

Once the design was finalized the device was fabricated in the MC2 cleanroom. The fabrication process is fairly simple as it requires a single ebeam exposition and reactive ion etching processes. A thin film of around 6-7 nm of NBTiN was sputtered on a sapphire substrate followed by the spin coating of PMMA ebeam resist. The designed pattern was then exposed by ebeam lithography, developed and etched using reactive ion etching.

Figure 10 below shows an optical microscope image of the resulting etched pattern. During the fabrication process some dust particles fell on the PMMA resist which prevented the etching of some regions of the pattern. This creates a short to the ground as the center line of the iCPW is now shorted to the ground plane rendering the device unusable. Due to this issue three out of four devices were lost and only a short straight line KI-TWPA could be measured.

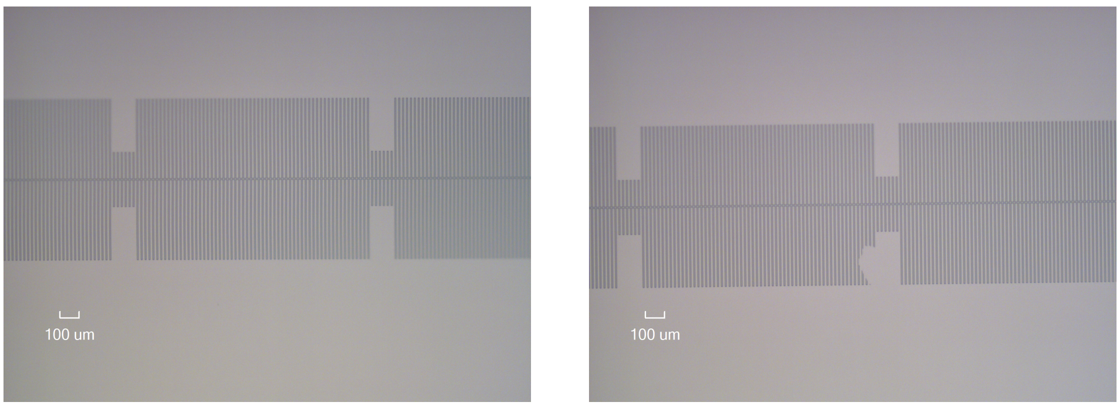

(a) (b)

Figure 10: Optical microscope images of the TWPA pattern etched in NbTiN. (a) View of the repeating supercell pattern. (b) Short to ground due to dust in the ebeam resist. Images courtesy of Mikael Kervinen.

3.2 Cryogenic Microwave Packaging

3.2.1 Printed Circuit Board

To connectorize the amplifier chip, a printed circuit board (PCB) was designed. The design uses CPWs to carry the signal to the chip. The waveguides are excited with a vertical SMA connector (SV Microwave 2921-40049-1S) to a via transition on one side of the PCB. The signal travels to the other side of the PCB which enables the CPW to be covered by a copper enclosure to improve electromagnetic shielding. To achieve good microwave performance, the CPW characteristic impedance must be designed as close to 50 Ω as possible to minimize the reflection coefficient described in (11). This design uses Rogers RO4350B as dielectric material with relative permittivity $\epsilon_r \approx 3.48$ and a thickness of 254 µm.

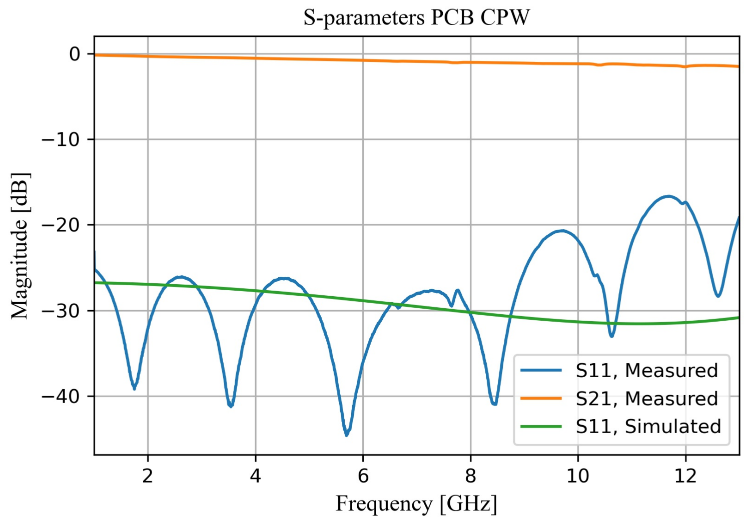

Figure 11: Measured reflection and transmission of the CPW, plotted against the simulated reflection obtained in COMSOL[3]

As can be seen from (10), the characteristic impedance of a transmission line is dependent on the inductance and capacitance of the line. These parameters can be tuned to achieve a characteristic impedance close to 50 Ω, which is done by changing the geometry of the CPW, see Figure 12b. The CPW with the via transition was simulated in COMSOL[3] and the resulting S_{11} from the simulations can be seen in Figure 11 together with the measurements of the actual fabricated PCB. The object measured is a PCB with the same CPW and via transition as the PCB used in the sample holder. The PCB was designed in KiCad and manufactured by Eurocircuit. The finished board can be seen in Figure 12a.

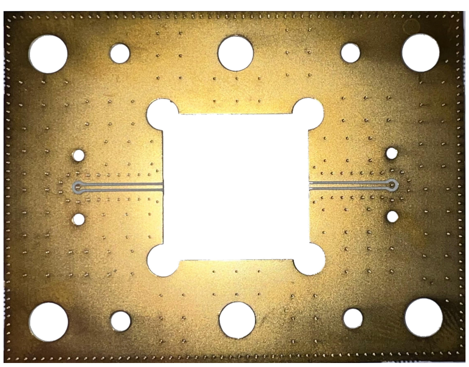

(a)

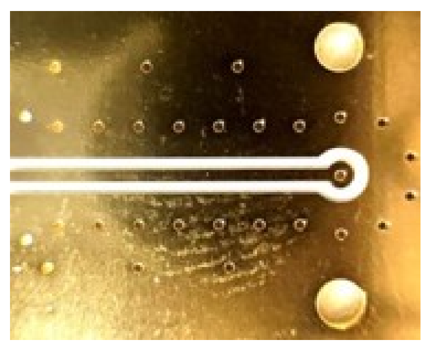

(b)

Figure 12: a) Bottom side of the finished PCB where the CPW is located. b) Close up of the signal trace showing the via transition to the CPW, tuned to achieve good microwave performance.

3.2.2 Copper Box

To shield the amplifier chip from radiation noise and provide good thermalization to the cryostat a copper box, seen in Figure 13, was designed to hold the chip and the PCB. Furthermore, the copper

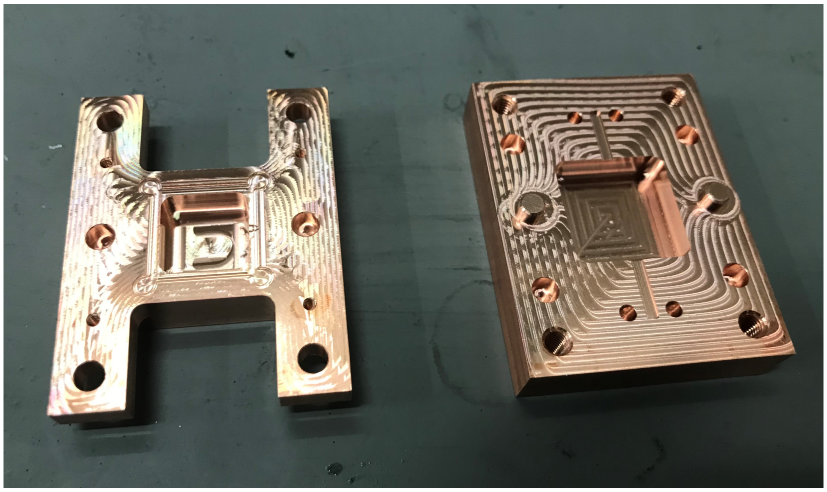

Figure 13: Inside view of the top piece (left) and bottom piece (right) of the copper box.

box was designed to remove unwanted resonance modes in the chip within the frequency range of interest. This was done by introducing a vacuum cavity beneath the chip with direct contact to the dielectric substrate. The dominant mode will then resonate in the combined medium of the chip and the cavity, with some effective permittivity. Because the air in the cavity has much lower relative permittivity ($\epsilon_r = 1$) than the relative permittivity of the chip ($\epsilon_r = 9.3$ or 11.5 depending on the rotation of the crystal) the resonant mode will experience a much lower effective permittivity than that of the chip. It will then oscillate at a higher frequency as seen in equation (22). In this way we can move the dominant mode up in frequency and out of the range of interest.

To calculate the necessary size of the cavity, the resonance frequencies where simulated in COMSOL [3]. The frequency range of interest for the TWPA was 3-14 GHz. Without the cavity the simulated lowest resonance frequency of the chip substrate was 3.9 GHz. With a cavity of side length 13 cm it could be increased to 14 GHz. The effect of the bottom cavity on the dominant mode can be seen in Figure 14. The cavity above the chip had to be considered as well as its dominant mode was a limiting factor for the chip. With a chip with a side length of 1.6 cm a top cavity of side length 1.84 cm was possible giving a resonance frequency of 11.6 GHz. Additionally, a tunnel connects the top cavity to the connectors to avoid shorting the CPW. This affects the impedence of the CPW and had to be taken into account in the design.

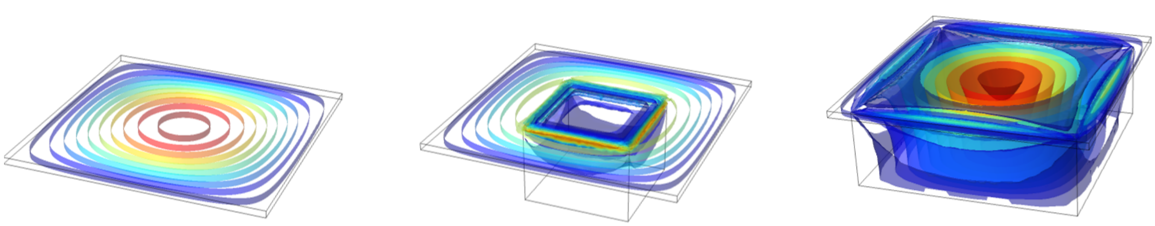

(a) (b) (c)

Figure 14: Dominant resonance mode for (a) the chip alone with a resonance frequency of 3.9 GHz (b) the chip with a cavity with side length 0.7 cm giving with a resonance frequency of 5.1 GHz (c) the chip with a cavity with side length 1.3 cm giving with a resonance frequency of 14 GHz. The field visualization is in each case for the dominant mode of the structure.

4 Experimental Set Up

Once the KI-TWPA was assembled inside the cryogenic microwave packaging, it can be characterized. The following section describes the measurement circuit and component specifications that enabled the measurement of the amplifier.

As KI-TWPA characterization was carried out at cryogenic temperatures, a setup capable of reaching such a regime was required. The cryogenic environment was provided by a dilution refrigerator cryostat which uses a mixture of ^{3}He and ^{4}He to cool down until 10 mK [17]. This temperature regime is obtained from room temperature through the stages indicated in Figure 15 which also displays the circuit used to provide our measurements.

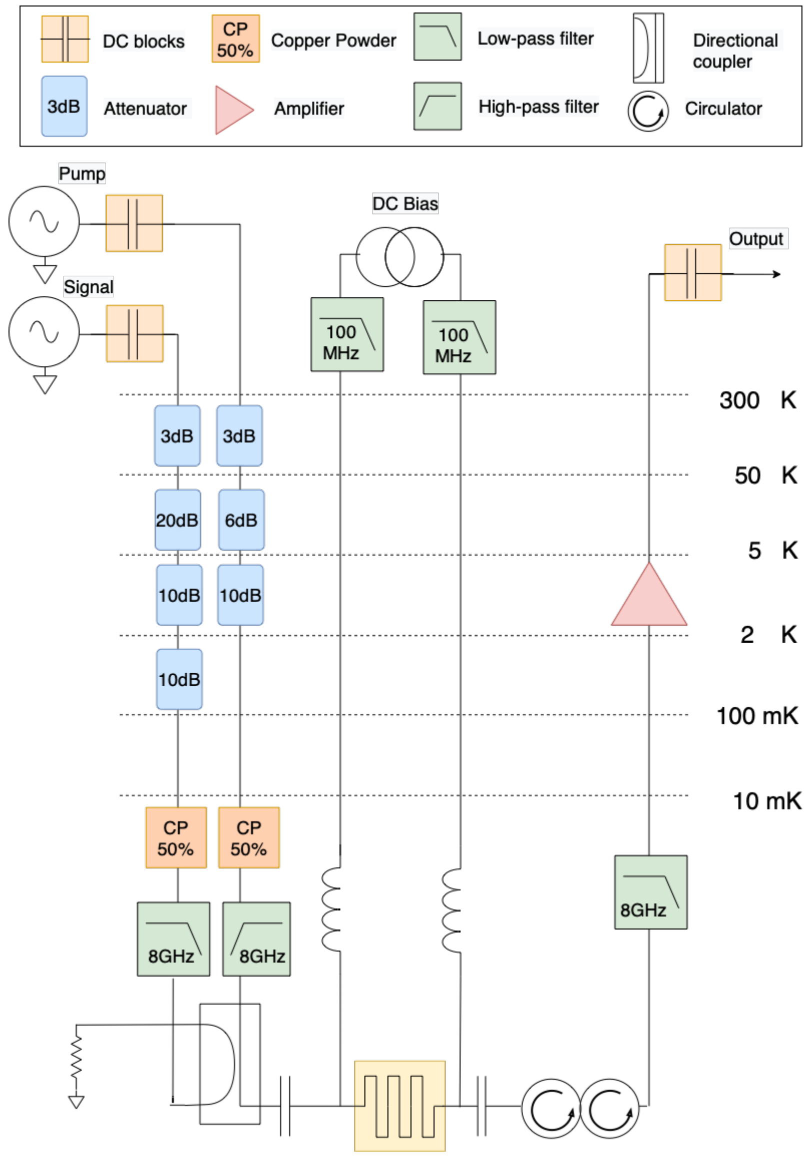

Figure 15: Sketch of the experimental setup.The KI-TWPA amplifier is represented by a zig-zag line, enclosed in a yellow square.

Each component of the circuit with corresponding serial number can be seen in Table 2. The instrument used for measuring transmission of the signal and pump line was the VNA P5004A from Keysight. DC biasing is done by a homemade current supply and the pump signal was supplied by a Rohde & Schwarz SGS100A RF source.

Component	**Model**	**Manufacturer**
DC block	BLK-18W-S+	Mini-Circuits
Attenuators	-	Provided with Bluefors cryostat
Copper powder filters (50%)	F4, F7	Made in-house
High-pass filter	ZHSS-8G-S+	Mini-Circuits
Low-pass filter	ZLSS-8G-S+	Mini-Circuits
Directional coupler	180120	Krytar
Bias Tee (after coupler)	BT-0025	Marki Microwave
Bias Tee (after TWPA)	BT-0018	Marki Microwave
Dual circulator	LNF-XXXXC4-12A	Low Noise Factory
Cryogenic LNA	LNF-LNC4-16B	Low Noise Factory
π-filters (DC supply)	4209-003LF	Tusonix

Table 2: Specifications of the components used to build up the measuring set-up indicated in Figure 15.

5 Measurement Results and Discussion

This section presents the KI-TWPA measurement results and discussion. First, the S21 stop-band measurement is compared to the simulated on previous sections. Then both the non-linearity inductance parameter I_* and the critical current I_c of the amplifier are portrayed giving insights on the superconducting properties of the sample. Finally, we provide a discussion of the amplifiers gain.

5.1 KI-TWPA stopband

As it has been stated in the previous sections, one of the key features to our amplifier is to have an stopband at a desired frequency. As seen in section 3.1.3, cascading the Sonnet supercell simulations through rf-scikit python library, we could predict that our stopband was expected 6.3 GHz. Therefore, one of the first measurements performed was to allocate such stopband in our actual circuit. To do so, we performed signal and pump measurements sweeping from 2 GHz to 10 GHz and from 2 GHz to 14 GHz. The former allows the comparison with the simulated result, whereas through the later the circuit behaviour can be understood.

Figure 16a shows the S21 parameter of forty four supercells cascaded plotted against the S21 circuit response. The observed offset difference in circuit S21 is because the red curve shows the S21 response of our circuit, not only the 44 supercelled amplifier, and is in agreement with the attenuation on schematics on Figure 15, ~ -40 dB. The other difference is the pass-band behaviour of the measured S21 that we attributed to the filters in the circuit. This difference can be seen in Figure 16b that shows the transmission of the pump line. The difference between signal and pump measurement is due to the difference in the measurement set up for each line. Both lines differ between 3 to 7 GHz because the pump line has a high pass filter, which the signal line does not have.

Another observed difference in Figure 16a between the curves is the right-shift between the expected stopband peak, predicted at 6.3 GHz, and the measured peak, located 6.6 GHz. When the shift-difference is quantified is found to be roughly a 4.5%, we attributed this shift to the kinetic inductance of the film as between the geometry used in the simulation and the actual device, the only parameter to be tuned experimentally in-situ is the inductance. It is left to be explained in the following section the impact of the inductance in the frequency shift. However, if we consider that the whole photonic cristal is as a LC resonator were the stopband corresponds to the resonance frequency given by $\frac{1}{\sqrt{LC}}$. According to 2.1 L is mainly given by the kinetic inductance. Then as $f \propto \sqrt{L_k}$ the inductance change can be estimated giving $L_{k-measured} = 0.9 L_{k-modelled}$. This variation can be attributed to the fabrication process as the kinetic inductance is highly dependant on the thickness of the deposited thin film [18].

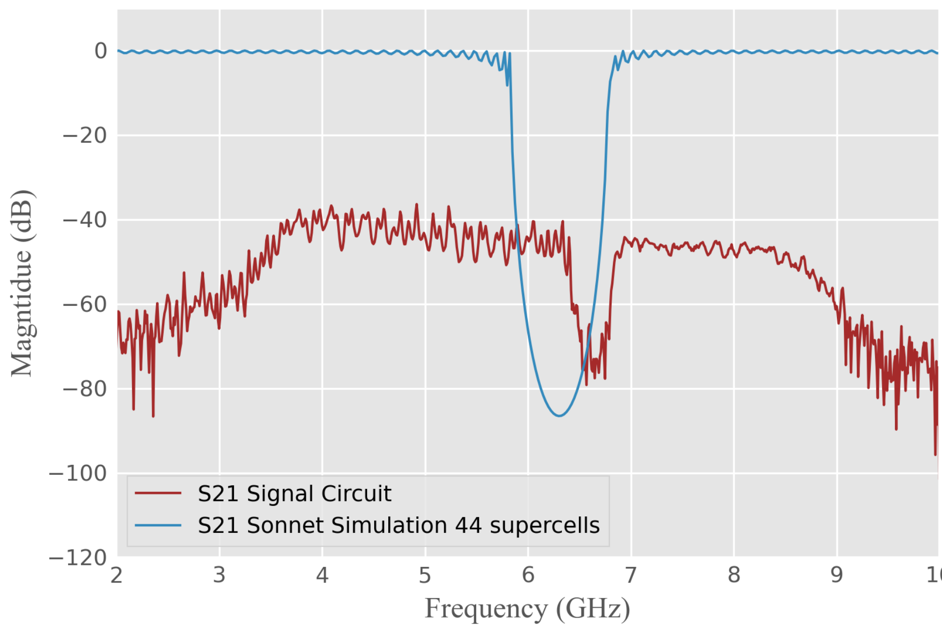

(a)

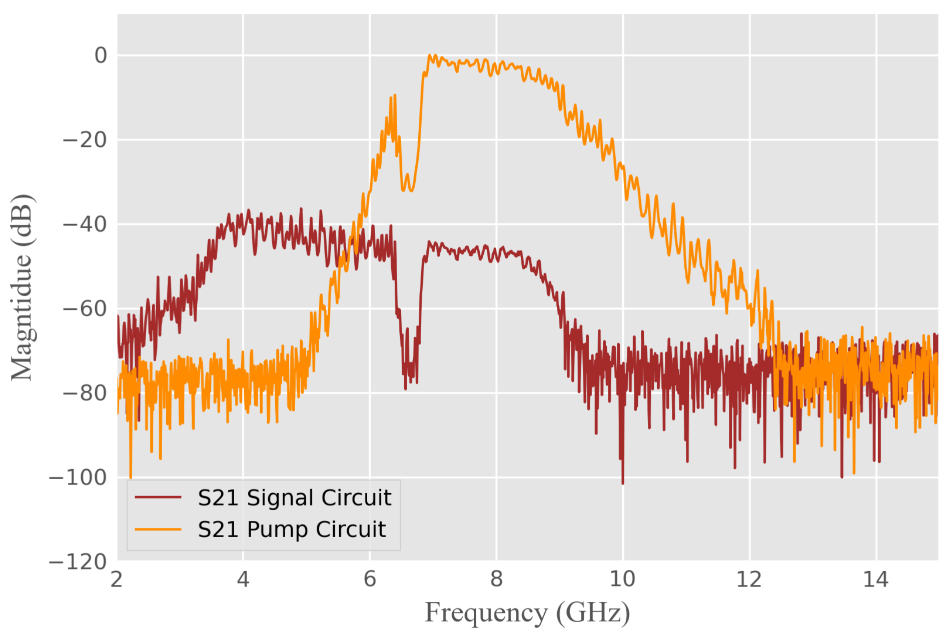

(b)

Figure 16: a) S21 parameter of the circuit with signal input (red) plotted against S21 parameter for forty-four supercells simulated through Sonnet (blue). b) S21 parameter of the circuit with signal input (red) plotted against S21 parameter of circuit with pump input (orange).

5.2 KI-TWPA Scaling Inductance Parameter I_*

This amplifier uses the high Kinetic Inductance of NbTiN to have 3WM amplification. In order to understand the device it is important to characterize the Kinetic inductance of our device. Recall eq. (15) that the Kinetic Inductance has a current dependence of the form $L_k(I) = L_0\left(1 + \frac{I^2}{I_*^2}\right)$.

As it has been seen in the previous section, the whole photonic cristal can be considered as a LC resonator were the stopband corresponds to the resonance frequency $\frac{1}{\sqrt{L_k C}}$. Furthermore, if we recall 7, the Kinetic Inductance can be modulated by applying a current. By applying a varying DC bias and observing the stopband shift in frequency, it was possible to retrieve the value of I_* (see 23).

$$\begin{aligned} f &= \frac{1}{\sqrt{CL_0\left(1 + \frac{I^2}{I_*^2}\right)}} \\ &\approx \frac{1}{\sqrt{CL_0}}\left(1 - \frac{I^2}{I_*^2}\right) \end{aligned} \qquad \Rightarrow \qquad \frac{|\Delta f|}{f} = \frac{1}{2}\left(\frac{I^2}{I_*^2}\right) \tag{23}$$

Figure 17 shows an S21 measure centered at the stopband frequency for varying DC current bias. The central features of the stopband are not affected by the current bias change, these are not kinetic inductance dependant, they are added on top of the stopband. On the other hand, the sidewalls of the stopband shift to lower frequencies. Indicating a frequency shift due to an increase in inductance, i.e the kinetic inductance due to the applied current bias. To characterise the frequency shift the S21 amplitude is taken around the Full Width Half Maximum (FWHM) of the stopband dip, this corresponds to an S21 amplitude of -55 dB. The frequency shift is then fitted with (23). Notice that the right side of the stopband shifts more in frequency, we attribute this to an added frequency dependence of total inductance L_0. The fitting yields characteristic currents of $I_*^{left} = 8.26$ mA and $I_*^{right} = 7.33$ mA. These values match well the expected values from Malnou et al. [1] around 7 mA.

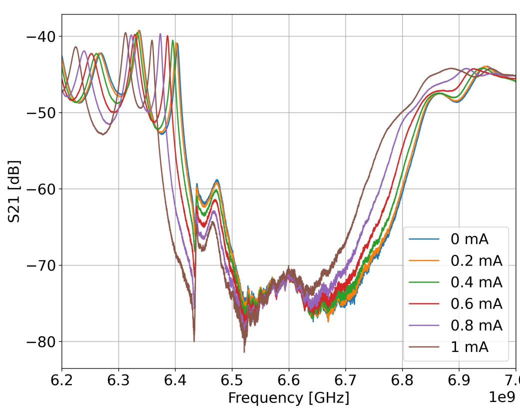

(a)

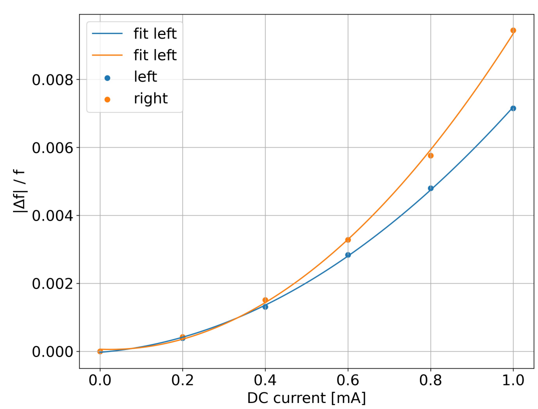

(b)

Figure 17: I_* measurements. (a) S21 amplitude centered at the stopband frequency for varying DC current values. (b) Fitted frequency shift experimental data.

5.3 KI-TWPA Critical Current $\mathrm{I_c}$

Another important parameter of the superconducting thin film is the critical current I_c as it gives the maximum current that the device can handle. Current biasing is crucial to the TWPA operation in 3WM, therefore it is important to know how much current can be applied while maintaining superconductivity.

Figure 18 shows the voltage drop across the DC bias lines for varying a dc bias current. For low current the slope of the IV curve is relatively flat, only a small resistance coming from the connecting cables is observed. At the critical current superconductivity breaks and the device becomes highly resistive, we observe a sharp voltage increase for a critical current of $I_c = 2.2$ mA which also matches well the result in [1] of 2.4 mA.

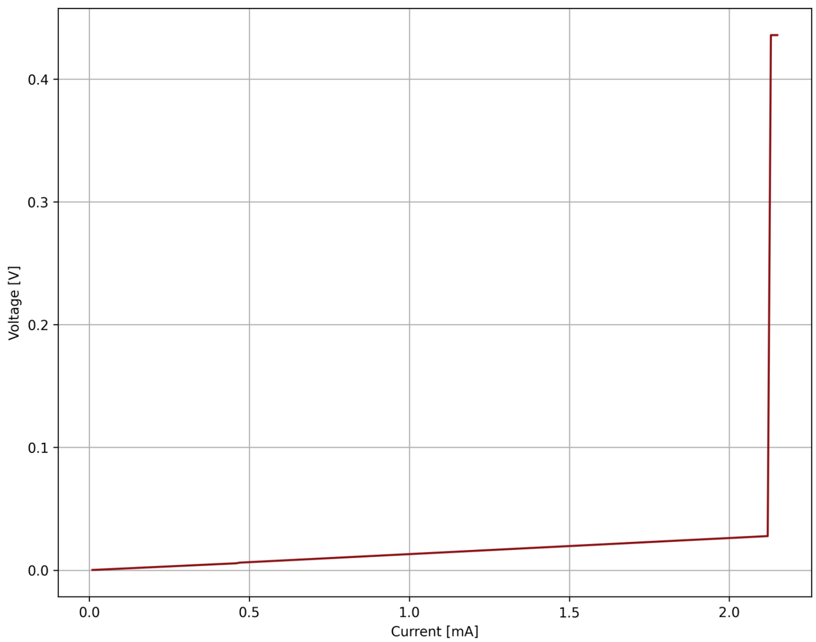

Figure 18: Voltage drop across the device for varying DC current bias.

5.4 KI-TWPA Gain

After characterising the superconducting sample, the performance of the device was measured. In principle, by applying a pump signal at a frequency on the right side (high frequency) of the stopband 3WM should occur and generate a gain region centered at a frequency half of the pump.

It was not possible to obtain any gain from the device. This is probably due to the fact that our device is not long enough. Dust particles on the ebeam resist created shorts to the ground for all our long devices and we had to measure a straight line TWPA with a transmission line of 1.5 cm.

Recall (21): $G_s(x) = \cosh^2(g_3 x)$. Where $g_3 = \frac{1}{8}\delta_L k_p$ and δ_L is the relative inductance variation due to the pump signal.

Notice that x, the length of the transmission line plays a key role in the gain as it grows exponentially with x. The total path length in [1] is 33 cm, in our case the path is 1.5 cm long. Since our device exhibits a similar I_* compared to [1] we can assume that the coefficient g_3 is approximately the same in our device. When introducing our path length in (21) we obtain an estimated gain of 0.02 dB while in [1] it is around 15 dB.

This low gain cannot be measured as it is comparable to the system noise and cannot be distinguished from it, thus explaining why we could not obtain gain. Our long device (zigzag pattern) was 12.5 cm long, repeating the estimation we could expect a gain of around 1.5 dB for said device. This is still not a satisfactory value for application in quantum computing but it would be measurable in our setup, thus validating or not our design.

6 Critical Summary and Outlook

In this project, we have designed and fabricated a KI-TWPA based on NbTiN thin film, including the design and fabrication of the cryogenic packaging for the chip. The design used the properties of periodic structures in a transmission line to create a stop-band at a desired frequency to enable phase-matching. Transmission measurements show close correlation between simulations and the actual data. The non-linearity of the kinetic inductance was measured and the characteristic current scale was obtained, showing a slight frequency dependence. Also, the critical current of the thin film was measured. Due to dust particles shorting the sample with the longest transmission line, only the sample with a short transmission line could be measured. Since the gain of the device increases with the length of the line, gain was not detected during measurements of the short sample. However, with a longer line, we expect that the device will show gain. A part from measuring new samples with longer transmission lines, it would be also interesting to characterizing the noise performance of the amplifier.

7 Acknowledgements

We would like to thank Attila Geresdi and Simone Gasparinetti for supervising this project and guiding us through it from start to finish. We also extend our thanks to Robert Rehammar for helping us design the microwave packaging and the CAD design of the pattern, Mikael Kervinen for fabricating the amplifier chip for us, François Joint for performing the wire bonding on the chip, Lars Jönsson for manufacturing the copper box as well as Ivo Cools and Vittorio Buccheri for helping us assemble the cryostat and helping us perform the measurements among other things. Without these people this project would not have been possible.

References

[1] M. Malnou, M. Vissers, J. Wheeler, *et al.*, "Three-wave mixing kinetic inductance traveling-wave amplifier with near-quantum-limited noise performance," *PRX Quantum*, vol. 2, p. 010 302, 1 Jan. 2021. DOI: 10.1103/PRXQuantum.2.010302. [Online]. Available: https://link.aps.org/doi/10.1103/PRXQuantum.2.010302.

[2] S. Inc. "Sonnet precision electromagnetics." (), [Online]. Available: https:%20//www.sonnetsoftware.com/.

[3] S. COMSOL AB Stockholm. "Comsol multiphysics® v. 5.6." (), [Online]. Available: www.comsol.com.

[4] J. Aumentado, "Superconducting parametric amplifiers: The state of the art in josephson parametric amplifiers," *IEEE Microwave Magazine*, vol. 21, no. 8, pp. 45–59, 2020.

[5] M. Esposito, A. Ranadive, L. Planat, and N. Roch, "Perspective on traveling wave microwave parametric amplifiers," *Applied Physics Letters*, vol. 119, no. 12, p. 120 501, 2021.

[6] B. H. Eom, P. K. Day, H. G. LeDuc, and J. Zmuidzinas, "A wideband, low-noise superconducting amplifier with high dynamic range," *Nature Physics*, vol. 8, no. 8, pp. 623–627, 2012.

[7] M. R. Vissers, R. P. Erickson, H.-S. Ku, *et al.*, "Low-noise kinetic inductance traveling-wave amplifier using three-wave mixing," *Applied Physics Letters*, vol. 108, no. 1, p. 012 601, 2016. DOI: 10.1063/1.4937922. eprint: https://doi.org/10.1063/1.4937922. [Online]. Available: https://doi.org/10.1063/1.4937922.

[8] P. Drude, "Zur elektronentheorie der metalle," *Annalen der physik*, vol. 306, no. 3, pp. 566–613, 1900.

[9] M. Cyrot and D. Pavuna, *Introduction to superconductivity and high-Tc materials*. World Scientific Publishing Company, 1992.

[10] C. J. Gorter and H. Casimir, "On supraconductivity i," *Physica*, vol. 1, no. 1-6, pp. 306–320, 1934.

[11] M. Tinkham, *Introduction to superconductivity*. Courier Corporation, 2004.

[12] J. R. Waldram, *Superconductivity of metals and cuprates*. CRC Press, 2017.

[13] W. Meissner and R. Ochsenfeld, "Ein neuer effekt bei eintritt der supraleitfähigkeit," *Naturwissenschaften*, vol. 21, no. 44, pp. 787–788, 1933.

[14] D. M. Pozar, *Microwave Engineering*, 4th ed. 111 River Street, Hoboken: John Wiley and Sons, 2011.

[15] D. K. Cheng, *Field and Wave Electromagnetics*, 2nd ed. Harlow Essex: Pearson Education, 2014.

[16] R. E. Collin, *Foundations for Microwave Engineering*, 2nd ed. Hoboken, New Jersey: John Wiley and Sons, 2001.

[17] H. Enss, *Low-Temperature Physics*. Springer-Verlag Berlin Heidelberg, 2005.

[18] R. M. L. Báez, "Coplanar stripline resonators for andreev quantum bits. microwave design and optimization," M.S. thesis, Chalmers University of Technology and KU Leuven, Gothenburg, Sweden, Jul. 2021.